Passive Separation Control on a Symmetric Airfoil via Elastic-Layer

C. Hafien[1†]; A. Bourehla[2] and M. Bouzaien[1]

[1] *Laboratory of mechanics of fluids, Faculty of Science of Tunis, 1060 Tunis cedex, Belvidère*
[2] *Aviation School of Borj El-Amri (ASBA), B.P 1142, Tunisia*

†*Corresponding Author Email: chedhli.hafien@gmail.com*

ABSTRACT

The passive control of flow-separation at averaged Reynolds Number ($Re=3.42\times10^5$) using self-adapting flexible-flaps in the upper side of the wing, is presented. The two-way Fluid-Structure Interaction (FSI) in an elastic-layer up on the airfoil (NACA 0012) is investigated numerically by Coupling between the Transient Structural and Fluid Flow (Fluent) in ANSYS-Workbench14.0. During the fluid-structure interaction, the transient deformation of the elastic-layer provokes the modification of the flow topology at large-scale. There are reductions of the size and intensity of the vortex-shedding and an increase in the Strouhal number. This explains the increase of the lift-to-drag ratio. The study of the flap flexibility shows that the deformation of the elastic-layer and the variation of aeronautical efforts are inversely proportional to the Young Modulus.

Keywords: Flexible-flaps; Young modulus; Two-way Fluid-Structure Interaction (FSI); Dynamic mesh.

1. INTRODUCTION

The Separation control has a tremendous impact in terms of economy and comfort on society. There are two methods for controlling the boundary-layer separation in order to optimize the flight performance: an active method which is more effective but more expensive, and a passive one that we must improve in order to maximize its effectiveness.

The phenomenon of flight at low Reynolds number prevails abundantly in nature, starting from as low as about $Re=10^3$ for insects like houseflies or mosquitoes, to around $Re=5\times10^4$ or more for birds like eagles (Venkataraman 2013). Similarly, in recent years the interest of flight at low Reynolds number increases in industry, as in the case of Unmanned Aerial Vehicles (UAVs) and Micro Aerial Vehicles (MAVs). But the airfoils functioning at low and average Reynolds numbers (i.e., $Re< 5\times10^5$) are sensitive to the laminar boundary layer separation, which can have a harmful effect on airfoil performance (Schlüter 2010; Yarusevych and Boutilier 2010) (see Fig. 1a and 1b). Among the techniques used in birds-flight in order to increase the lift and/or decrease the drag is the separation control through the interaction between the feathers and the boundary-layer flow on the wing (see Fig. 2).

Bechert *et al*. (2000) experimentally investigated the separation control by self-activated movable flap set on the upper surface of the airfoil (HQ41) at a Reynolds number of $Re=10^6$. The experiment showed that the small flap (having a length of about 12% of the airfoil chord length) can increase lift by 10%, and a flap length of 22% resulted in an increase of 18% in the maximum lift. Similar results were found in other studies (Hafien *et al*. 2013; Schatz *et al*. 2004; Traub and Jaybush 2010; Mazellier and Kourta 2011).

The influence of different configurations of self-adaptable flexible flaps (hairy flaps) on the flow around an airfoil (NACA 0020) is investigated experimentally at low Reynolds number ($Re=7.7\times10^3$) by Brücker and Weidner (2013) (see Fig. 3). The PIV (Particule Image Velocimetry) measurement shows that the hairy flap coating has largely reduced the region of backflow and has prevented stall.

A poro-elastic layer of hairy medium can be used as passive flow actuator (Gosselin and de Langre 2011). This problem is studied numerically by Favier *et al*. (2009), a cilia-like hairy coating attached at a two dimensional circular cylinder at Reynolds number $Re=200$ yielding an average drag reduction of 15% and a decrease of lift fluctuations by about 40%, associated to a stabilization of the wake.

Venkataraman and Bottaro (2012) numerically studied the passive control of flow separation on a symmetric aerofoil (NACA0012) with a dense poro-elastic coating, as a two-way coupled fluid-
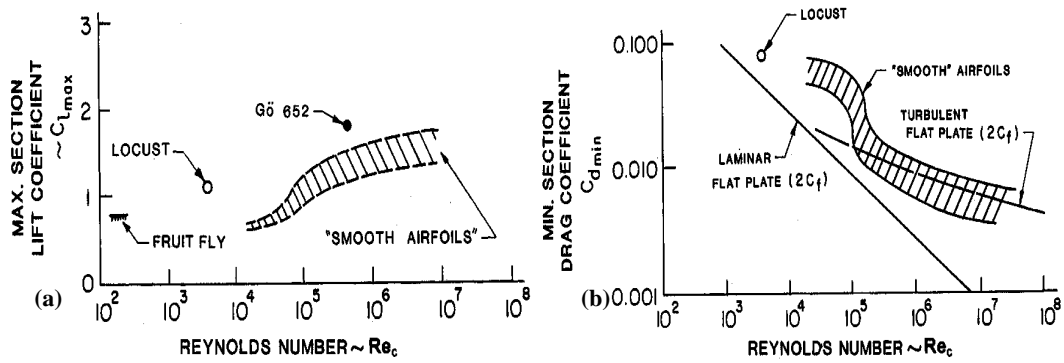
Fig. 1. Dependence of the lift (a) and the drag (b) coefficients, on Reynolds number (Mueller 2001).

Fig. 2. Flow control on the upper side of the eagle wing, by interaction between the feathers and the flow in the separated boundary-layer.

structure interaction problem. For a very low Reynolds number flow, these passive actuators, are capable of producing a high lift enhancement of more than 30% (for attack angle of 22°) and a moderate lift increase of around 8% (for 70°); a noteworthy drag reduction of around 9% (for 45°) and a moderate drag reduction of around 5% (for 70°).

Fig. 3. NACA0020 airfoil with hairy-flaps (Brücker and Weidner 2013).

In this work, we investigated numerically the passive separation control around an airfoil (NACA 0012) at high attack angle (20°), using an elastic-layer (flexible-flaps) placed in the upper surface of the airfoil. The numerical model used to study the two-way problem of the Interaction between the flexible-flaps and the flow in the post-stall regime is presented in the first section. In the second section we studied the impact of self-adaptive flexible-flaps on aerodynamic performances by structural and frequency analyses. Finally, the effect of flap elasticity (Young Modulus) is investigated.

2. NUMERICAL SIMULATION

The passive separation control problem using the elastic-layer is studied numerically by ANSYS-Workbench. In this section we present:

- The numerical model to solve the fluid domain equations (ANSYS-Fluent).

- The characteristics of the elastic-layer (flexible-flaps) (ANSYS-Mechanical)

- The Fluid-Structure Interaction (FSI) problem by coupling between transient structural (ANSYS-Mechanical) and fluid flow (ANSYS-Fluent).

2.1 Equations and Numerical Model

The governing equations of the unsteady flow of an incompressible viscous fluid past an airfoil (NACA0012) are the continuity (1) and the conservation of momentum (2) equations. The rate of change term and the convective term are on the left hand side of the Eq. (2), and the diffusion term on the right hand side.

$$\vec{\nabla}\vec{v} = 0 \tag{1}$$

$$\rho\left(\frac{\partial \vec{v}}{\partial t} + \vec{v}(\vec{\nabla}\vec{v})\right) = \vec{F} - \vec{\nabla}p + \vec{\nabla}(\bar{\bar{\tau}}) \tag{2}$$

Where p is the static pressure, $\vec{v}$ is the velocity vector, $\vec{F}$ represents an external body force field

and $\overline{\overline{\tau}}$ is the stress tensor (described below):

$$\overline{\overline{\tau}} = \mu \left[\left(\vec{\nabla}\vec{v} + \vec{\nabla}\vec{v}^T \right) \right) - \frac{2}{3}\vec{\nabla}\vec{v}I \right].$$ Where; μ is the

dynamic viscosity, and I is the identity tensor. By using the Finite Volume Method (FVM), the Navier-Stokes Eq. (2) is integrated over a Control Volume (CV) in order to obtain algebraic equations that are resolvable numerically. With regard to the dynamic meshes, the integral of the Eq. (2) on the control volume (CV) by applying Gauss divergence theorem, is written as follows in Eq. (3).

$$\rho \frac{d}{dt}\int_{CV}(\vec{v})dV + \rho\int_A (\vec{v}(\vec{v}-\vec{v}_m))d\vec{A}$$
$$= \int_{CV}\vec{F}dV - \int_A pd\vec{S} + \int_A \overline{\overline{\tau}}d\vec{S} \tag{3}$$

Where $\vec{v}_m$ is the velocity of the moving mesh.

In the finite volume method, the fluid domain is divided into a number of cells (grid). The First-order discretization of the convection term for a flow that is aligned with the mesh is able to give acceptable results. But for complex flows (as in our case), we use the «second-order-upwind» discretization to obtain better results. The pressure-velocity coupling is made using PISO algorithm.

The turbulence model used is the Shear-Stress Transport *SST-kw* model (Menter 1994). It consists of the *kw* model in the near-wall region and the *kε* model in the free-stream region. These characteristics make the *SST-kw* model more accurate and reliable for separated flow, than the standard *kw* model. The transport equations for the *SST-kw* Model are the Eqs. (4) and (5).

$$\frac{\partial}{\partial t}(\rho k) + \frac{\partial}{\partial x_i}(\rho k v_i)$$
$$= \frac{\partial}{\partial x_j}\left(\Gamma_k \frac{\partial k}{\partial x_j}\right) + \tilde{G}_k - Y \tag{4}$$

and

$$\frac{\partial}{\partial t}(\rho w) + \frac{\partial}{\partial x_j}(\rho w v_j)$$
$$= \frac{\partial}{\partial x_j}\left(\Gamma_w \frac{\partial w}{\partial x_j}\right) + G_w - Y_w + D_w \tag{5}$$

Where: $\tilde{G}_k$ and G_w represent respectively the generation of k and w. Γ_k And Γ_w represent the effective diffusivity of k and w, respectively. Y_k And Y_w represent the dissipation of k and w. D_w represents the cross-diffusion term.

The effective diffusivities for the *SST-kw* model are given by:

$$\Gamma_k = \mu + \frac{\mu_t}{\sigma_k}; \ \Gamma_w = \mu + \frac{\mu_t}{\sigma_w}$$

Where σ_k and σ_w are the turbulent Prandtl numbers for k and w, respectively. The turbulent viscosity, μ_t

is computed as follows:

$$\mu_t = \frac{\rho k}{w} \frac{1}{\max\left[\frac{1}{a^*}, \frac{SF_2}{0.31w}\right]}$$

Where S is the strain rate magnitude, and the coefficient a^* damps the turbulence viscosity causing a low-Reynolds number correction. It is given by:

$$a^* = \frac{0.144 + \text{Re}_t}{6 + \text{Re}_t}; \ \text{Re}_t = \frac{\rho k}{\mu w}$$

and $F_2 = \tanh\left(\varphi_2^2\right)$

where $\varphi_2 = \max\left[2\frac{\sqrt{k}}{0.09wy}, \frac{500\mu}{\rho y^2 w}\right]$

$$\sigma_k = \frac{1}{F_1/1.176 + (1-F_1)}$$

$$\sigma_w = \frac{1}{F_1/2 + (1-F_1)/1.168}$$

Where $F_1 = \tanh\left(\varphi_1^4\right)$

$$\varphi_1 = \min\left[\max\left(\frac{\sqrt{k}}{0.09wy}, \frac{500\mu}{\rho y^2 w}\right), \frac{4\rho k}{1.168 D_w^+ y^2}\right]$$

$$D_w^+ = \max\left[2\rho\frac{1}{1.168w}\frac{\partial k}{\partial x_j}\frac{\partial w}{\partial x_j}, 10^{-10}\right];$$

Where y is the distance to the next surface, and D^+_w is the positive portion of the cross-diffusion term: The *SST-kw* model is based on both the standard *kw* model and the standard *kε* model. To blend these two models together, the standard *kε* model has been transformed into equations based on k and w, which leads to the introduction of a cross-diffusion term defined as:

$$D_w = 2(1-F_1)\rho\frac{1}{1.168w}\frac{\partial k}{\partial x_j}\frac{\partial w}{\partial x_j}$$

The term $\tilde{G}_k$ represents the production of turbulence kinetic energy, and is defined as:

$$\tilde{G}_k = \min\left(\frac{\mu_t}{4}\left(\frac{\partial u_i}{\partial x_j} + \frac{\partial u_j}{\partial x_i}\right)^2, 10Y_k\right);$$

$$G_w = \frac{0.113F_1 + 0.44}{a^*\upsilon_t}\cdot\left(\frac{0.111 + \text{Re}_t/2.95}{1 + \text{Re}_t/2.95}\right)\tilde{G}_k$$

The term Y_k represents the dissipation of turbulence kinetic energy:

$$Y_k = 0.09\left[\frac{\left(4/15 + (\text{Re}_t/8)^4\right)\left(1 + 1.5F(M_t)\right)}{1 + (\text{Re}_t/8)^4}\right]\rho kw$$

The term Y_w represents the dissipation of w:

$$Y_w = \left(-0.0078 F_1 + 0.0828 \right)$$

$$-0.135 \left[\frac{4/15 + (\mathrm{Re}_t/8)^4}{\left(1 + (\mathrm{Re}_t/8)^4\right)} \right] F(M_t) \rho w^2$$

2.2 Computational Model

We consider an airfoil (NACA0012) with chord c operating at angles of attack α, and placed in airflow-filed at Reynolds number Re=3.42×10^5. The computational domain consists of 5c upstream and 10c downstream, the height and the width of the domain are 10c and 0.01c respectively (the width of the domain is equal to the wing span).

The airfoil was equipped with array of flexible-flaps. Two configurations were studied: an elastic-layer consisting of 8 identical and equidistant flaps (named «flp-id») (Bourehla *et al.* 2015) and an elastic-layer consisting of 8 flaps with increasing lengths and spaces along of the airfoil-chord (named « flp-vr »), See Fig. 4a and 4b.
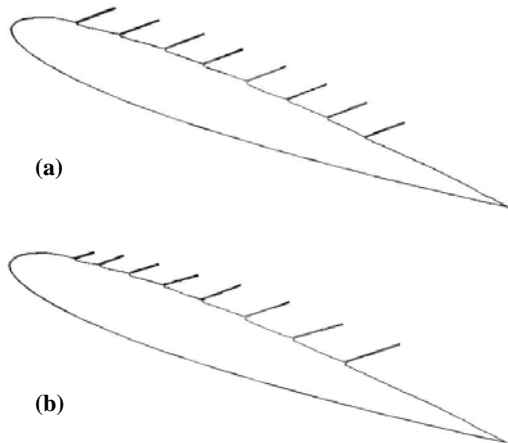

(a)

(b)

Fig. 4. NACA 0012 airfoil with elastic-layer: (a) « flp-id » configuration (Bourehla *et al.* 2015); (b) « flp-vr » configuration.

The boundary conditions are « velocity inlet » and « pressure outlet » respectively for the inlet and outlet of the computational domain, and « symmetry » for the left and right faces. A sweep mesh method is used for the 3D-simulation of flow-field, where the mesh type of free faces (the left and right faces) is triangular. The computational mesh provides 424 nods around the airfoil and 224 around the flexible-flaps. The total number of cells wedge is about 38576. In the elastic-layer, the dynamic mesh model is used to simulate the automatic movement of the flexible-flaps (see Fig. 5). The displacements of these flaps are large compared to the size of the grid cells, thus we use the smoothing and remeshing methods.

2.3   Characteristics   of   Elastic-Layer (Flexible-Flaps)

The   elastic-layer   must   have   the   principal characteristics which emulate the properties of bird-feathers (Favier *et al.* 2009; Venkataraman 2013).

In this work, the elastic-layer consisted of an array of self-activated flexible-flaps. The optimization of these flaps traits (dimension, position, spacemen, flexibility…) is very significant so that they react well with the separated boundary layer. The separated boundary layer's thickness increases along the airfoil chord. Thus, the movements of flaps near the trailing edge are important compared to those near the leading edge. For this reason, the effect of the increasing of the flap-length along the airfoil-chord is investigated.

There are 8 flaps coating more than 60% of the upper surface of the airfoil, starting 0.1 units of length after the leading edge –similar to the case already studied by Venkataraman and Bottaro (2012)- (see Fig. 4a and 4b). The length of the kth flap is L_k (where k=1, 2…8), l=0.01c and e=0.002c are the width and thickness of each flap respectively, and (x_k-x_{k-1}) the space between the k and k-1 flaps, (see Fig. 6).

In the « flp-id » configuration (Bourehla *et al.* 2015), all flaps are of the same length and space $L_k = x_{k+1}-x_k$ =0.08c. In the « flp-vr » configuration, the lengths and positions of flaps are defined by the arithmetic progressions (6) and (7).

$$L_{k+1} = L_k + r \tag{6}$$

$$x_{k+1} - x_k = L_{k+1} - r \tag{7}$$

Where: L_1= 0.04c; x_1= 0.1c and r= 0.01c.

The flaps' elasticity is defined using the Hooke law:

$$\overline{\overline{\sigma}} = E \overline{\overline{\varepsilon}} \tag{8}$$

Where: $\overline{\overline{\sigma}}$ is the stress tensor; E is the Young Modulus; and $\overline{\overline{\varepsilon}}$ is the deformation tensor. The physical characteristics of the flexible-flaps are: the Young Modulus E varies from 2.5×10^6 to 10^{9}Pa; the Poisson Coefficient equal to 0.35 and the density ρ_{flp}=2550Kg.m^{-3}. The flap's geometry is created by «ANSYS Design Modeler» then exported to «transient structural» (ANSYS-Mechanical). A structured quadratic mesh is used for these flaps (see Fig. 6).

2.4 Two-way FSI problem

The 3D Navier-Stokes equations of incompressible and unsteady airflow are simulated by ANSYS-Fluent, and the deformations of flexible-flaps are simulated by ANSYS-Mechanical. The Fluent solver computes the fluid pressure applied on flexible-flaps and the ANSYS-mechanical solver determines the flexible-flaps deformations under the influence of the fluid pressure. Besides, the fluid solution affects the structural deformation, and the structural deformation affects the fluid solution (Fig. 7). Thus the two-way FSI (Fluid-Structure Interaction) is investigated by Coupling between the «Transient Structural» and «Fluid Flow (Fluent)» in ANSYS- Workbench 14.0.

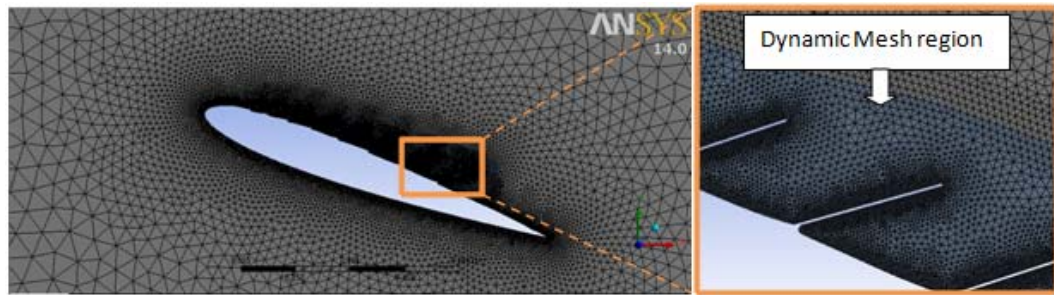In   ANSYS-Workbench,   co-simulation   was performed   between   (ANSYS-Mechanical)   and

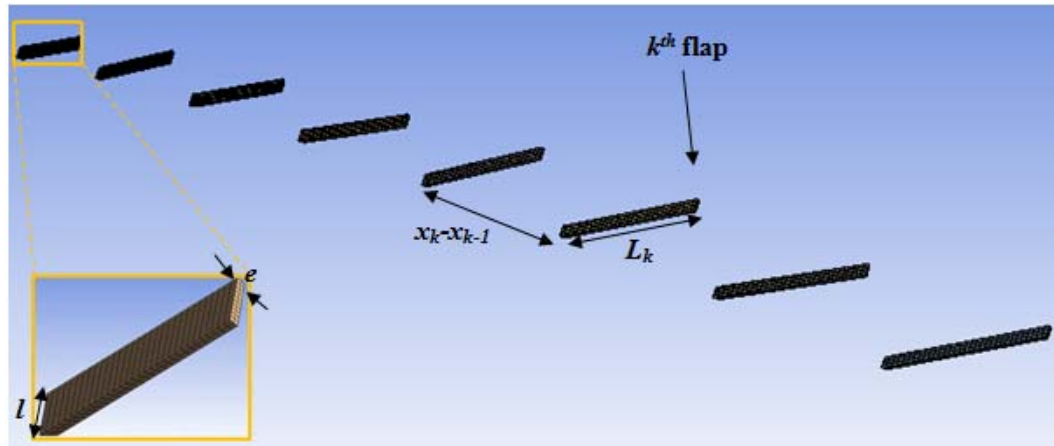**Fig. 5. Mesh around NACA 0012 airfoil with elastic-layer (ANSYS-Fluent).**

Fig. 6. Geometry and mesh of flexible-flaps; (elastic-layer for the « flp-vr » configuration) (ANSYS-Mechanical).
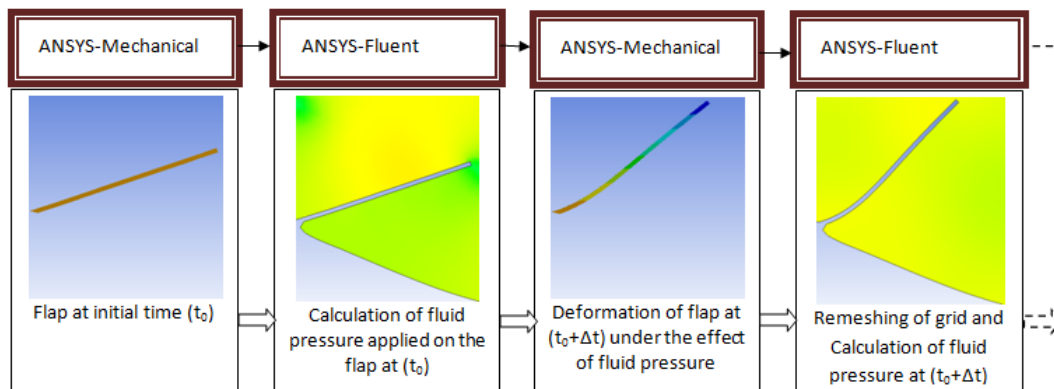

Fig. 7. Two-way FSI by coupling between ANSYS-Mechanical and ANSYS-Fluent.

(fluid-flow Fluent); both models get developed independently. Each model requires its proper mesh, boundary condition, analysis options, and output options, etc (Kaled *et al*. 2013). The data transfer between both solvers is realized through the fluid-structure interfaces. The coupling system service manages this coupled analysis (ANSYS-Workbench).

3. NUMERICAL RESULTS

3.1 Without Control Case

We first studied the without control case for an unsteady flow around an airfoil (NACA0012) at Reynolds number equal to 3.42×10^5. Fig. 8a and 8b show respectively the variation of lift and drag coefficients with angle of attack α. Good agreement is obtained between ANSYS-Fluent results and the experimental results from the literature, (the values obtained by ANSYS-Fluent are time-averaged values). The curve of lift-coefficient contains two peaks; the first peak was obtained at an angle of attack about 10° to 14°, and the second at 45°. A brutal fall of lift-coefficient is obtained for angle of attack varies between 15° and 20°, this decrease is caused by a great separation region upper side of the wing (Critzos *et al.* 1955; Sheldahl and Klimas
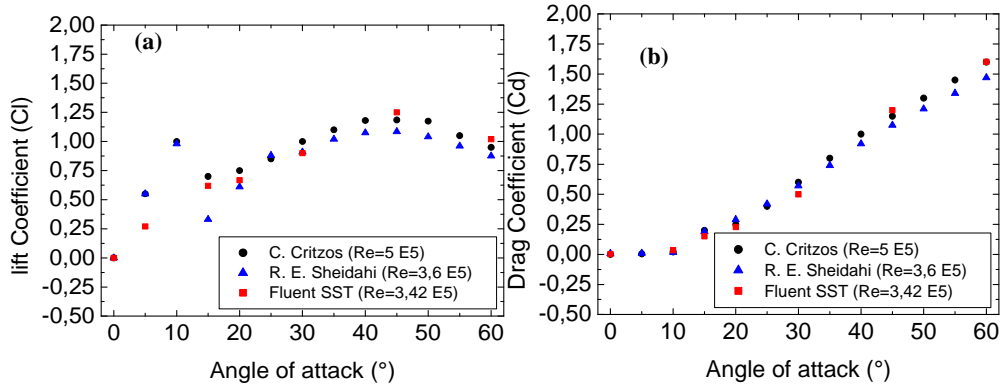
Fig. 8. Validation of time-averaged values of (a) lift and (b) drag coefficients for the NACA0012 airfoil at various angles of attack, obtained from ANSYS-Fluent.
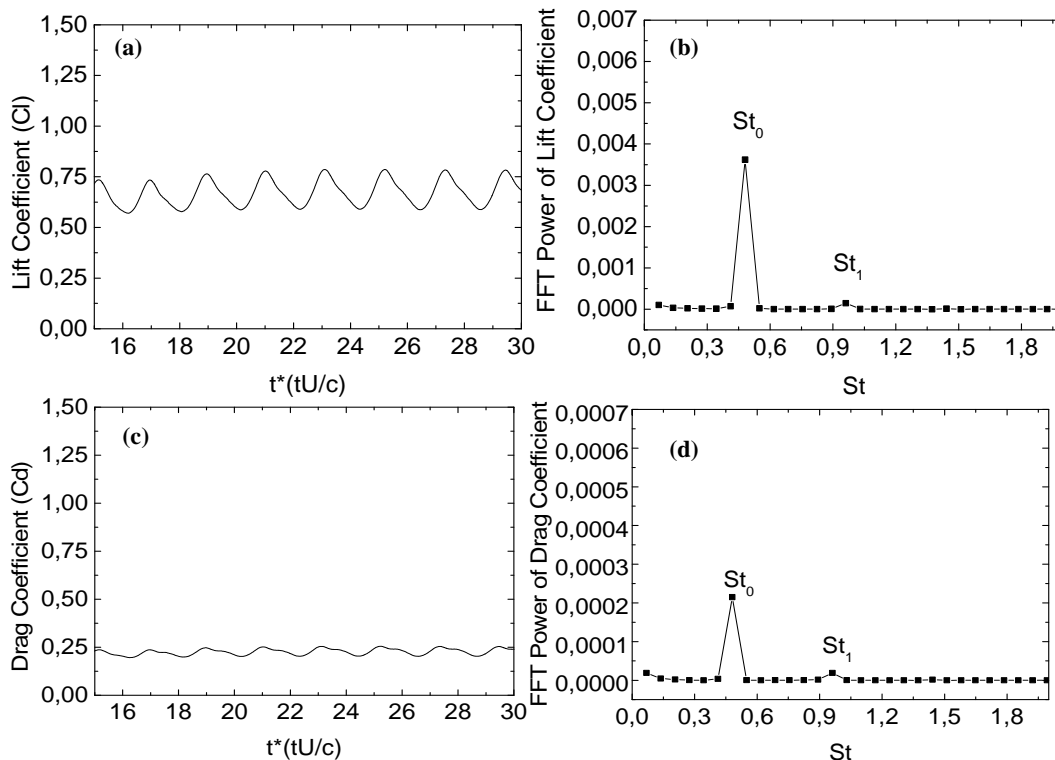

Fig. 9. Evolution of lift (a) and drag (c) coefficients signals as a function of dimensionless time; FFT power of lift (b) and drag (d) coefficients signals as a function of Strouhal number.

1981). In the continuation of this work, the angle of attack α is fixed at 20°, in order to study the characteristics of the flow at this angle and to control it.

In Fig. 9a and 9c, the lift and drag coefficients signals are presented as a function of dimensionless time t^* ($t^*=tU/c$; where t is the time, U the free-stream velocity and c is the chord-length of the airfoil). These signals are varied periodically with a dimensionless temporal period $T^*=2.083$ ($T^*=TU/c$; where T the temporal period of lift and drag coefficients signals for without control case) corresponding to principal Strouhal number

$St_0=0.48$. The average value of the lift coefficient is equal to 0.683 with positive and negative fluctuations respectively of 15% and 13.6% in each period. Likewise for the drag coefficient, the average value is equal to 0.231 with positive and negative fluctuations of 10.5% and 11.7% respectively in each period. A secondary small peak appears in the FFT curve, this peak corresponding to secondary Strouhal number $St_1=0.961$ (see Fig. 9b and 9d). This result shows the deformed signal characteristics.

In Fig. 10, we present the dependence between the evolution of flow topology and the aeronautical
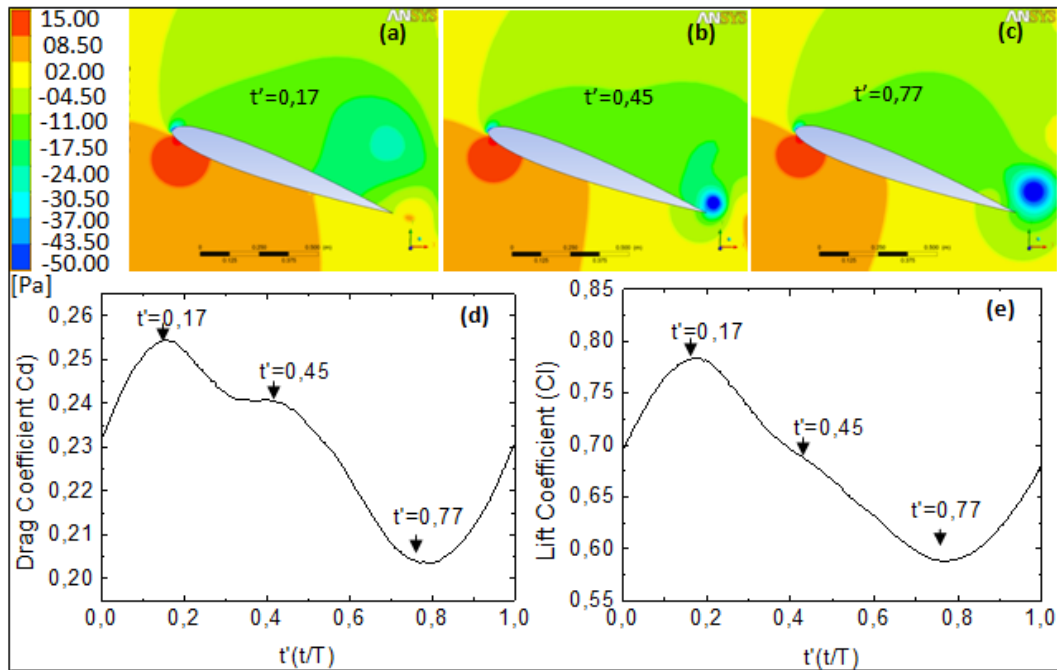
Fig. 10. Dependence between the evolution of flow topology –top- and the aeronautical efforts –bottom-, for one period. (a, b, c): respectively the pressure contours at *t'* equal to 0.17, 0.45 and 0.77; (d, e) respectively the drag and lift coefficients signals.

efforts, for one period. We notice the presence of both vortices; a great vortex (main vortex) situated upper on the airfoil, and a small vortex (secondary vortex) contra-rotating with precedent, located downstream of trailing edge. During the presence of main vortex, the lift/drag coefficients achieve these maximum values at *t'*=0.17 (*t'*=t/T). As time progresses, the vortex size reduces and the lift/drag coefficients as well decrease and reach these average values at *t'*=0.45. In this time, a second vortex contra-rotating with the precedent, is created downstream of trailing edge. This secondary vortex increases as time progresses, which induces a decrease of lift/drag coefficients to minimum values at *t'*=0.77.

3.2 With Control Case

In this section, we study the passive control separation using an elastic-layer consisting of 8 flexible-flaps. Both configurations are used (« flp_id » (Bourehla *et al.* 2015) and « flp_vr »). The effect of Fluid Structure Interaction on the: aeronautical efforts, Strouhal number and on the flow topology is investigated at Young Modulus *E* equal to 5×10^5 Pa. The influence of deformation of elastic-layer (flaps' movements) on the vortex-shedding characteristics is presented.

3.2.1 Effect of Two-Way FSI on the Aerodynamic Efforts

A significant increasing of lift coefficient is obtained after control. The time-average values of lift coefficients are 1.029 and 1.134 estimating an increase of 53% and 69.49% respectively for « flp_id » and « flp_vr » configurations. The time-average values of drag coefficients are 0.281 for

« flp_id » configuration and 0.319 for « flp_vr » configuration; this gives an increase respectively to 25.16% and 21.5% of the lift-to-drag ratio (see Fig. 11a and 11c). The passive separation control by Fluid Structure Interaction (FSI) provokes the modification of signal characteristics of aerodynamic coefficients; a decrease of lift and drag fluctuations by 15% for « flp_id » configuration, associated to a stabilization of the flow. The new dimensionless temporal period for both configurations is *T'**=0.792*T**, then the new principal Strouhel number is *St'*=0.606 and the secondary is St'_1=1.212 (see Fig. 11b and 11d).

Fig. 12 presents the flow topology around the airfoil with control, at moments: *t'*=0.17, *t'*=0.35 and *t'*=0.56. These moments are respectively relative at maximum, average and minimum values of lift and drag signals in one period, for both configurations. Compared to the without control case, the prominent size reduction of the main vortex is clear in this Figure. At the same time, a decrease of secondary vortex intensity is observed. This reduction changes the characteristics of vortex-shedding in the airfoil wake.

3.2.2 Effect of FSI on the Flow Topology

Fig. 13 presents the pressure contours and the streamlines velocity around the airfoil, at different moments for one period. For *t'* varied between 0 and 0.35 the main vortex is created on the airfoil. This vortex moves in the same direction of flow-field but with a lower speed.

At *t'*=0.35 the secondary vortex contra-rotating with the main vortex is created downstream of trailing edge. The main vortex disappears at *t'*=0.45, and the size of the secondary increases. Both vortices
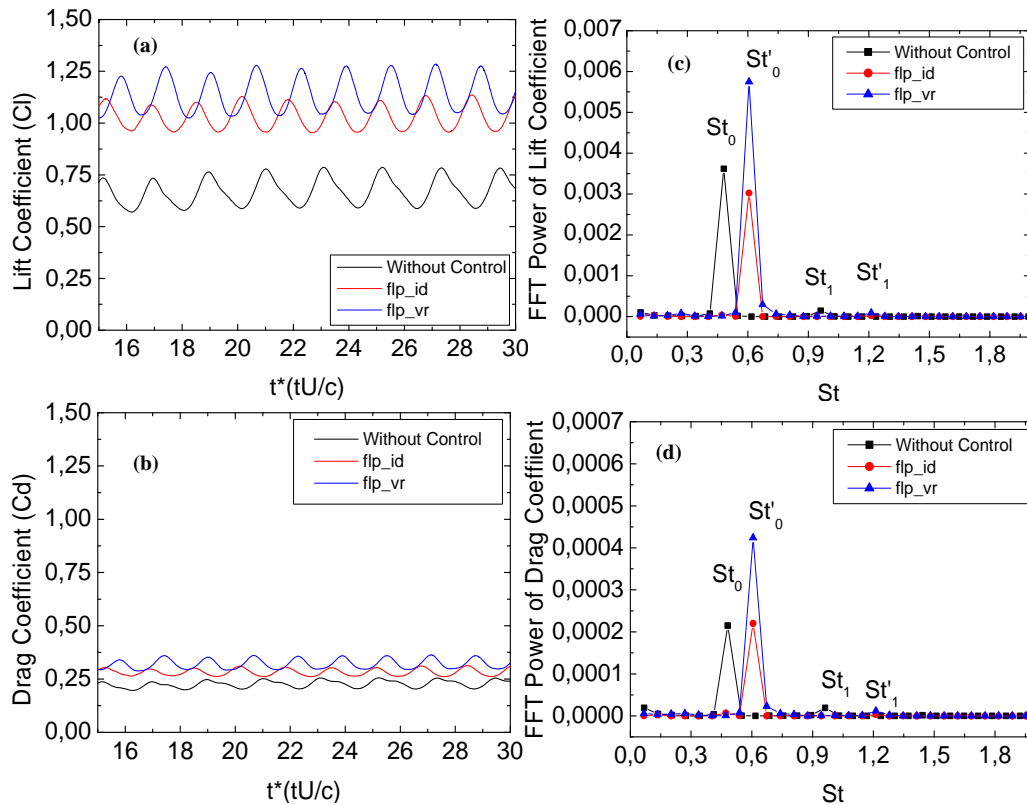
Fig. 11. Comparison between the without and with control cases: Evolution of lift (a) and drag (c) coefficients signals as a function of dimensionless time; FFT power of lift (b) and drag (d) coefficients signals as a function of Strouhal number.
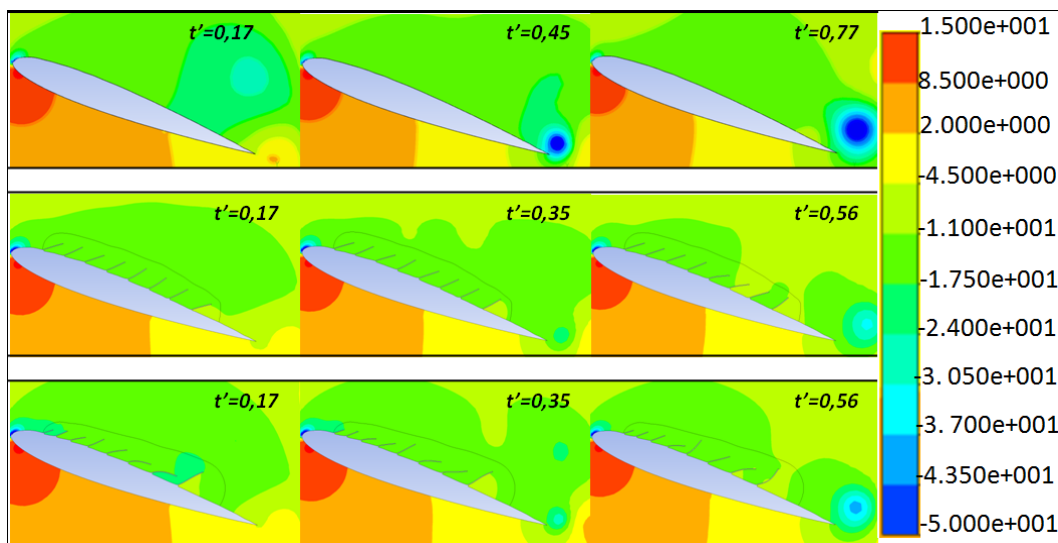

Fig. 12. Pressure contour around the airfoil: (top) without control; (Middle) « flp_id » configuration and (bottom) « flp_vr » configuration. The moments *t'*=0.17, *t'*=0.35 and *t'*=0.56 are respectively relative to maximum, average and minimum values of lift and drag signals in one period, for with control case.

move in the same direction of flow-field. The vortex shedding in wake region is formed by the interaction between these contra-rotating vortices (main and secondary vortices). This physical phenomenon repeats itself at *t'*=1 for uncontrolled case and repeats at *t'*=0.792 for « flp_id » and « flp_vr » configurations. This explains the increase of Strouhal Number from St_0=0.48 in the uncontrolled case to St'_0=0.606 in the controlled case.

In both configurations of controlled case, the elastic-layer pushes the main vortex to the top, and reduces the intensity of secondary vortex. We notice the creation of small vortices under side of the main vortex (around the flaps) (see Fig. 14).

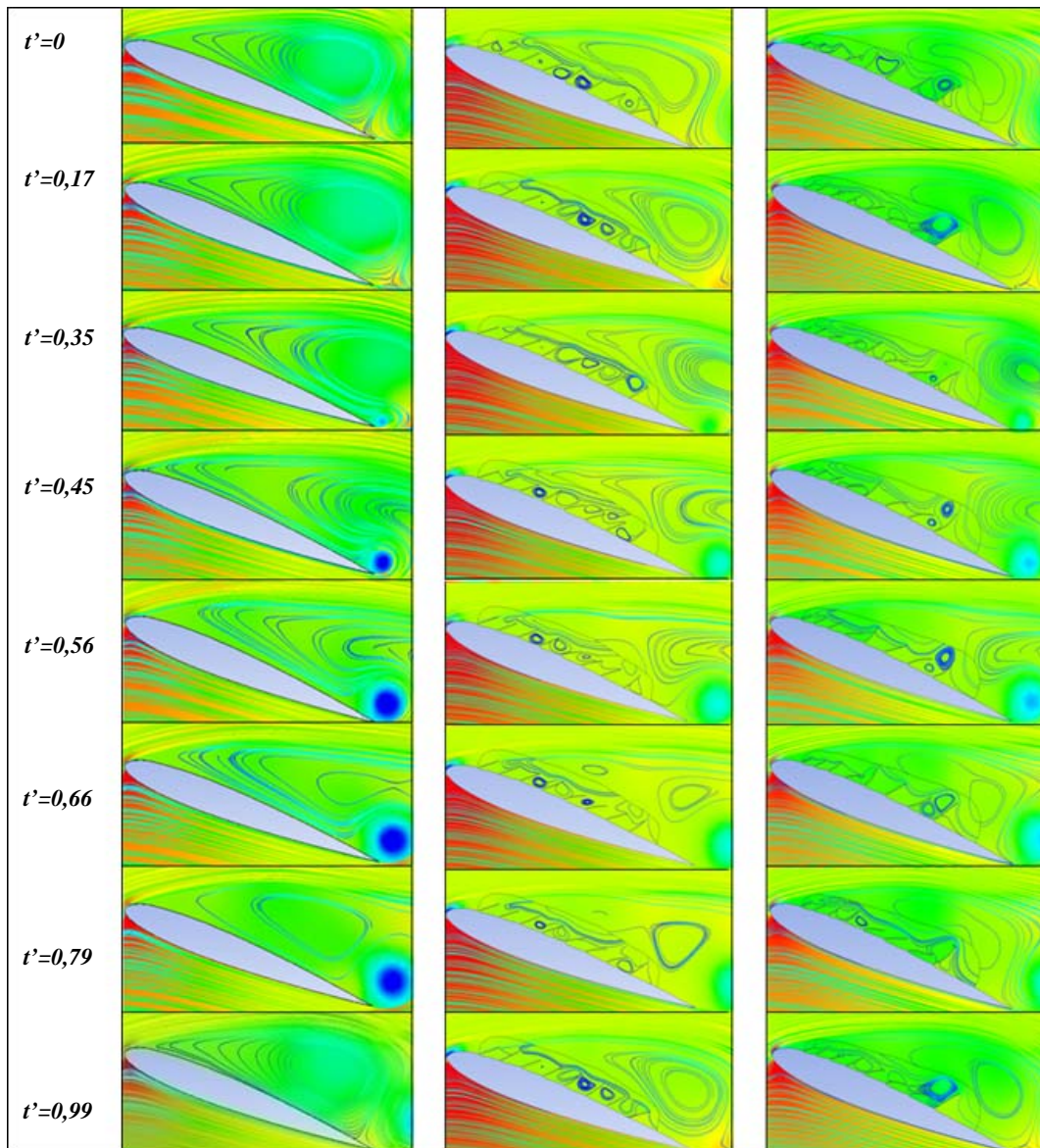|			
$t'=0$			
$t'=0,17$			
$t'=0,35$			
$t'=0,45$			
$t'=0,56$			
$t'=0,66$			
$t'=0,79$			
$t'=0,99$			

Fig. 13. Sequence of creation and movement of vortices for one period: (left) without control; (middle) « flp_id » configuration (Bourehla *et al.* 2015), and (right) « flp_vr » configuration.

These small vortices move through the elastic-layer (from the rotational movements around each flap) then react with the main and secondary vortices in the airfoil wake. Hence, a modification of vortex shedding is showed in the wake region. Fig. 15a, 15b and 15c show a reduction in longitudinal and transversal directions of the wake; this is caused by the reduction of temporal period (increase of Strouhal number) and the decrease of vortices sizes. The narrowing in the vertical direction of the wake involves an amelioration of aerodynamic efforts.

3.2.3 Relation between the Elastic-Layer Deformation and the Flow Topology

Because of the interaction between the range of flaps (elastic-layer) and the flow, each flap oscillates around an equilibrium position. These oscillations induce a transient overall deformation of the elastic-layer (see Fig. 16a and 16b).
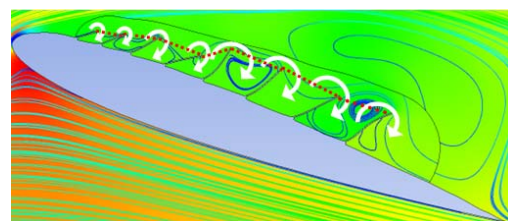

Fig.14. movements of small vortices through the elastic layer.

The dimensionless deformation of the elastic-layer is defined by Eq. (9):

$$\psi = \frac{\sum\limits_{k=1}^{N}(y_k(t) - y_k(0))}{Nc} \qquad (9)$$

Where $y_k(0)$ and $y_k(t)$ are the vertical coordinates of extremity of the kth flap respectively at: initial and t

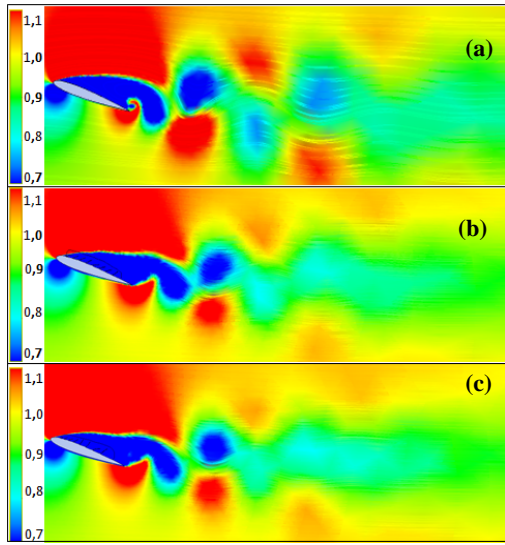moments; N the flaps number (N=8 in our case) and c is the airfoil chord-length.

Fig. 15. Streamlines dimensionless-velocity (v/U; where v is the flow velocity); (a) without control; (b) «flp_id » configuration and (c) « flp_vr » configuration.
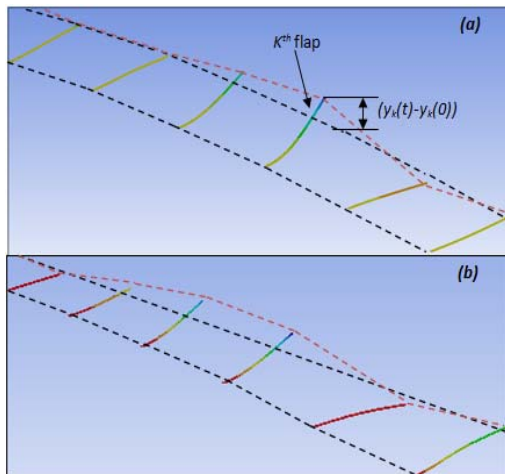

Fig. 16. Instantaneous deformation of elastic-layer during the Fluid-Structure Interaction (black dashed line: initial form, red dashed line: form at t moment); (a) «flp_id » configuration (Bourehla *et al.* 2015), and (b) « flp_vr » configuration.

Fig. 17a shows the deformation curve of elastic-layer for both configurations («flp_id» and «flp_vr»). This curve is pseudo-periodic as a function of dimensionless time t^*, each period contains secondary fluctuations. The oscillation amplitude of deformation in the «flp_vr» configuration is more important compared to the «flp_id» configuration.

The Fast Fourier Transform (FFT) of the dimensionless deformations shows the existence of three dominant dimensionless frequencies for each configuration (f^*=c/Ut: dimensionless frequency).
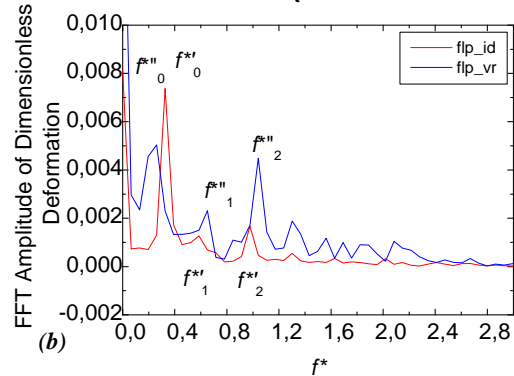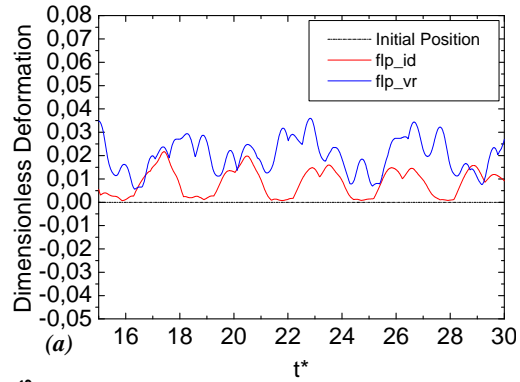

Fig. 17. (a) Dimensionless deformation of the elastic-layer as a function of t^*; (b) FFT Amplitude of dimensionless deformation of the elastic-layer as a function of dimensionless frequency f^*.
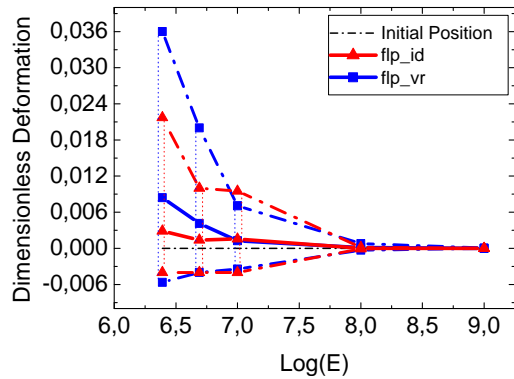

Fig. 18. Dimensionless deformation of elastic-layer as a function of decimal logarithm of Young modulus E; (solid lines) time-averaged values, (dashed lines) positive (top) and negative (bottom) fluctuations.

For «flp_id» configuration, the principal dimensionless frequency (which is corresponding to the principal deformation) is $f^{*'}_0$=0.33, the second and third dimensionless frequencies (corresponding to secondary fluctuations) are $f^{*'}_1$=0.6 and $f^{*'}_2$=0.976 respectively. Same, for the «flp_vr» configuration, the principal dimensionless frequency is $f^{*''}_0$=0.3 and the second and third frequencies are $f^{*''}_1$=0.67 and $f^{*''}_2$=1.05 respectively.

The comparison of the results obtained by the Fourier analyses of lift and drag coefficients signals

(without and with control) with those obtained for the deformation of elastic-layer shows the effect of flexible-flaps on the vortex-shedding characteristics in the wake region. The principal Strouhal number of the flow for the uncontrolled case (St_0=0.48) is greater than the principal dimensionless frequency of deformation of the elastic-layer in the controlled case for both configurations ($f*'_0$=0.33 and $f*''_0$=0.3). This is caused by the resistance of flexible-flaps. The flow topology in the controlled case is changed under the effect of the secondary fluctuations of the layer deformation, the values of second and third dimensionless frequencies ($f*'_1$=0.6 and $f*'_2$=0.976; $f*''_1$=0.67 and $f*''_2$=1.05) are well close to the values of principal and secondary Strouhal numbers of flow in the controlled case (St'_0=0.606 and St'_1=1.212).
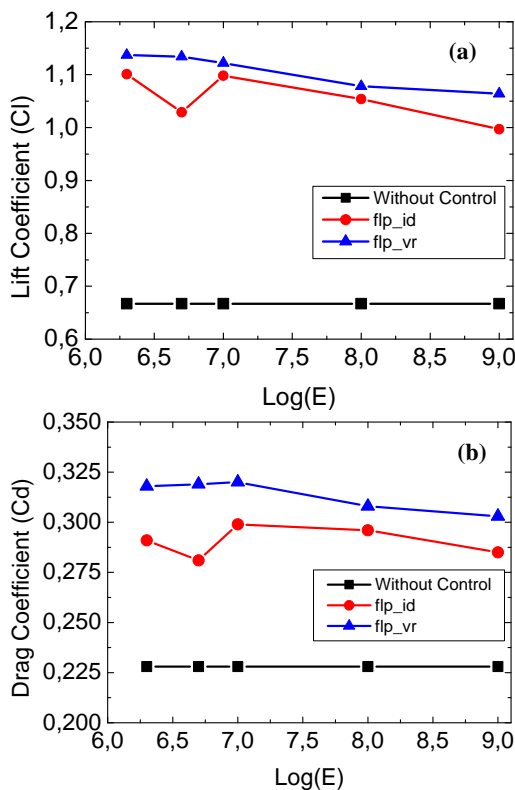

Fig. 19. Dependence of lift (a) and drag (b) coefficients on the decimal logarithm of Young Modulus *E*.

3.3 Parameter study "Young Modulus"

In this section, we explore the effect of flaps flexibility (Young Modulus *E*) on the elastic-layer deformation, and consequently on the aerodynamic efforts.

The value of deformation of the elastic-layer, as a function of the Young modulus *E*, is presented in Fig. 18, where *E* varies from 2.5×10^6Pa to 10^9Pa. The time-averaged value and the positive and negative fluctuations of this deformation, decrease when the Young modulus *E* increases. A strong deformation of the elastic-layer is obtained for $2.5\times10^6 \leq E \leq 10^7$, in this interval the « flp-vr »

configuration layer is more deforming than that of the « flp-id » configuration. For $E >10^8$, the deformation is negligible; therefore, practically there is not an elastic-layer, and no two-way Fluid-Structure Interaction. Fig. 19a and 19b present respectively the evolution of lift and drag coefficients with the Young Modulus *E*, for « flp-id » and « flp-vr » configurations. It is obvious that the values of aerodynamic efforts are higher for the « flp-vr » configuration compared to the other configuration.

For both configurations the lift and drag coefficients are inversely proportional to Young modulus *E*. For « flp-id » configuration, there is a fall of the aerodynamic efforts at $E =5\times10^6$. These results show the dependency between the flexibility of elastic-layer and the aerodynamic efforts. The more the layer is deformable, the more the amelioration of aerodynamic efforts is significant.

4. CONCLUSION

In this paper, we have studied the two-way Fluid-Structure Interaction (FSI) problem, using an elastic-layer, in order to control the unsteady flow separation on the upper side of NACA0012 airfoil, at Reynolds Number based on the chord-length c of Re=3.42×10^5. The coupling between «ANSYS-Fluent» and «ANSYS- Mechanical» is used to simulate this problem.

Two configurations were used for this passive control: the « flp_id » configuration (elastic-layer consisted of 8 flexible-flaps with length and spacing identical), and the « flp_vr » configuration (elastic-layer consisted of 8 flexible-flaps with length and spacing increases along of the airfoil-chord).

An increase of lift coefficient of 69.49% and 53% respectively for « flp_vr » and « flp_id » configurations is obtained. The interaction between the flexible-flaps and the flow upper side of the airfoil results in a transient deformation of elastic-layer. This induces a modification of flow topology. An increase of Strouhal number of flow and a reduction of size and intensity of vortex shedding are obtained in the wake region.

The investigation of elasticity of flaps shows that the amelioration of aerodynamic efforts is more significant for the more deformable layers (the lift and drag coefficients are inversely proportional to the Young modulus *E*, and the lift coefficient is larger for the « flp_vr » configuration compared to the other configuration; this is caused by the most important deformation of the layer of this configuration).The elastic-layer remains non-deformable from E=10^8.

REFERENCES

Bechert, D. W., M. Bruse, W. Hage and R. Meyer (2000). Fluid Mechanics of Biological Surfaces and their Technological Application. *Natur-wissenschaften,* 87, 157–171.

Bourehla, A., C. Hafien and T. Lili (2015).

Simulation numérique de l'interaction fluide-structure d'un profil d'aile équipé de volets élastiques. *22ème Congrès Français de Mécanique, Lyon, 24 au 28 Août 2015*

Brücker, C. and C. Weidner (2013). Separation control via self-adaptive hairy flaplet arrays. *ERCOFTAC international symposium Unsteady separation in fluid-structure interaction Mykonos, Greece, 17-21.*

Critzos, B. C. C., H. H. Heyson and R. W. J. Boswinkle (1955). *Aerodynamic characteristics of naca 0012 airfoil section at angles of attack from 0° to l80°. National Advisory* Committee for Aeronautics Technical Note. 3361: 20000510 077.

Favier, J., A. Dauptain, D. Basso and A. Bottaro, (2009). Passive separation control using a self-adaptive hairy coating. *J. Fluid Mech* 627, 451–483.

Gosselin, F. P. and E. de Langre (2011). Drag reduction by reconfiguration of a poro-elastic system. *Journal of Fluids and Structures* **27**, 1111–1123.

Hafien, C., A. Bourehla and T. Lili, (2013). Simulation numérique d'un écoulement autour d'un profil d'aile muni d'un volet poreux. *21ème Congrès Français de Mécanique, Bordeaux, août 26-30.*

Khalid, S. S., L. Zhang, X. W. Zhang and K. Sun (2013). Three dimensional numerical simulation of a vertical axis tidal turbine using the two-way fluid structure interaction approach. *Journal of Zhejiang University SCIENCE A* 14(8), 574-582.

Mazellier, N. and A. Kourta (2011). Amélioration des performances aérodynamiques d'un profil au moyen d'un actionneur passif auto-adaptatif. *20ème Congrès Français de Mécanique Besançon, 29 août au 2 septembre.*

Menter, F. R., (1994). Two-Equation Eddy-Viscosity Turbulence Models for Engineering Applications. *AIAA Journal* 32, 1598–1605.

Mueller, T. J. A. D., J. D. (2001). An Overview of Micro Air Vehicle Aerodynamics, in Fixed and Flapping Wing Aerodynamics for Micro Air Vehicle Applications. *AIAA, Progress in Astronautics and Aeronautics 1-10.*

Schatz, M., T. Knacke and F. Thiele (2004). Separation Control by Self-Activated Movable Flaps. *42th AIAA Aerospace Sciences Meeting and Exhibit 5-8 January /Reno, NV.*

Schlüter, J. U. (2010). Lift Enhancement at Low Reynolds Numbers Using Self Activated Movable Flaps. *Journal of Aircraft* 47(1), 348-351.

Sheldahl, R. E. and P. C. Klimas (1981). Aero-dynamic Characteristics of Seven Symmetrical Airfoil Sections Through 180 Degree Angle of Attack for Use in Aerodynamic Analysis of Vertical Axis Wind Turbines. *SAND80-2114 Unlimited Release Printed March.*

System Coupling User's Guide, ANSYS Help System, Workbench, ANSYS-Workbench 14.0.

Traub, L. W. and L. Jaybush (2010). Experimental Investigation of Separation Control Using Upper-Surface Spoilers. *Journal of Aircraft* 47(2), 714-717.

Venkataraman, D. (2013). *Flow control using a porous, compliant coating of feather-like actuators.* MS thesis, University of Genova, Department of Civil, Chemical and Environmental Engineering, Italy.

Venkataraman, D. and A. Bottaro (2012). Numerical modeling of flow control on a symmetric aerofoil via a porous, compliant coating. *Physics of Fluids* 24, 093601.

Yarusevych, S. and M. S. H. Boutilier (2010). Vortex Shedding Characteristics of a NACA 0018 Airfoil at Low Reynolds Numbers. *40th Fluid Dynamics Conference and Exhibit, 28 June- 1 July 2010, Chicago, Illinois, AIAA 4628.*